IEEE Photonics Journal
An IEEE Photonics Society Publication

Open Access

Accurate Pixel-to-Pixel Alignment Method With Six-Axis Adjustment for Computational Photography

Volume 10, Number 3, June 2018

Shou-Bo Zhao
Ming-Yang Ma
Cong Guo

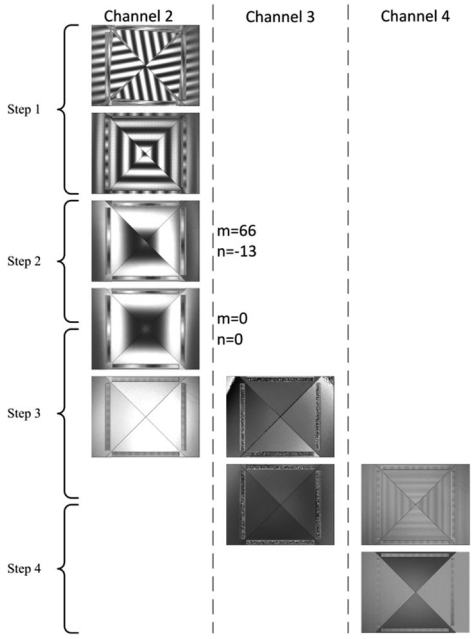

DOI: 10.1109/JPHOT.2018.2839093
1943-0655

IEEE photonics SOCIETY

IEEE

Accurate Pixel-to-Pixel Alignment Method With Six-Axis Adjustment for Computational Photography

Shou-Bo Zhao, Ming-Yang Ma, and Cong Guo

The Higher Educational Key Laboratory for Measuring and Control Technology and Instrumentations of Heilongjiang Province, Harbin University of Science and Technology, Harbin 150080, China

DOI:10.1109/JPHOT.2018.2839093

Manuscript received April 19, 2018; revised May 15, 2018; accepted May 17, 2018. Date of publication May 21, 2018; date of current version June 18, 2018. The work was supported by the Natural Science Foundation of Heilongjiang Province under Grant QC2016067. Corresponding author: Shou-Bo Zhao (e-mail: shoubozh@126.com).

Abstract: Computational photography has been a new research focus over the last two decades. Most of the computational imaging applications involve pixel-to-pixel correspondence adjustment between the spatial light modulator and the sensor. In this study, an accuracy pixel-to-pixel alignment method with six-axis adjustment is proposed. Specifically, the relations between the moiré fringe distribution and the six degree of freedom (DoF) displacements are characterized. A special pattern called five-grating pattern is designed for monitoring and adjusting the six DoF displacements in a four-step alignment procedure. Finally, the experimental results verify the performance of the proposed method by discussing the alignment accuracy.

Index Terms: Alignment, computational imaging, moiré techniques, Fourier optics and signal processing.

1. Introduction

Computational photography has been a new research focus over the last two decades, in that flexible imaging is achieved by modulating the imaging ray with the spatial light modulator (SLM) [1]–[4]. Most of computational imaging applications, such as digital micromirror device (DMD) camera profile measurement, dual-coded hyperspectral imaging, temporal pixel multiplex imaging, high dynamic range imaging and intra-pixel optical feature detection, involve pixel-to-pixel correspondence adjustment on the object-image conjugate architecture composed of the sensor and the SLM, i.e., accurate pixel-to-pixel alignment is one of the key technologies in computational photography [5]–[9]. However, it is rather difficult to align the SLM with the sensor on a pixel-precise basis, due to their micrometer-level sizes [2].

Moiré fringe is a phenomenon that occurs in the superposition of two repetitive structures such as two gratings [10]. The two gratings with the layout of the period or quasi-period structures appear as black-and-white or gray-scale patterns. Moiré fringe distribution will change with the frequency and slope deviations in the two grating patterns. In the case that the geometrical layout of the two gratings are given, the variation of the moiré fringe distribution can reflect the spatial relative displacement of the two gratings. The reflection have been applied in many fields such as lithography alignment, displacement determination and x-ray imaging [11]–[13]. Therefore, moiré

fringe analysis is a feasible approach to solve the alignment problem in computational photography, while the SLM and CCD as two gratings can be used to produce Moire fringes. In recent years, there are many excellent optical alignment methods based on moiré fringe analysis, which mainly focus on various lithography techniques [14]–[19]. These methods can be mainly summarized by several characteristics. By overlaying two sets of gratings with slightly different periods that are etched on the mask, moiré fringes with phase difference which determines the relative linear displacement of two masks are generated [14]–[16]. The type of method requires that grating pattern possesses design flexibility. Obviously, it is not suitable for CCD and SLM as two gratings in computational photography, which elements are changeless on micrometer scale. Another characteristic is that interference architecture and laser device assist in generating interference patterns or measuring relative displacement of two masks [17]–[19]. However, the moiré fringe is generated by superposing the sensor and the image of SLM in the object-image conjugate architecture. The object-image conjugate architecture as adjusted object is immutable in computational imaging system. In other words, these methods are limited by this object-image conjugate architecture.

In the object-image conjugate architecture, the SLM plane is imaged at the sensor plane by the relay optics. The SLM can be regarded as one grating by controlling the programmable filter array to form black and white line patterns, and the sensor can be regarded as another grating by using the subsampling technique. When the image of SLM pattern is superposed on the sensor pattern, the produced moiré fringe will be displayed in the screen. Ri Shien proposed a three-step alignment procedure that the spatial relative displacement between the SLM and the sensor are adjusted to perform pixel-to-pixel alignment by using the phase-shifting moire method [5], [20]. The spatial relative displacement between the SLM and the sensor involves the adjustment in six degree of freedom (DoF) motions including three linear displacements on the horizontal axis x, the vertical axis y, the optical axis z and three angular displacements on pitch angle, yaw angle, roll angle. So far, it has been the most effective method for pixel-to-pixel alignment in computational photography. However, the accuracy of three-step alignment procedure is always limited by the following shortcomings. The roll-yaw-pitch angular displacement are adjusted by observing straight form of moiré fringe. And 6-axis adjustment were not provided with quantizable monitoring object.

The moiré fringes are generated by two superposed gratings with different frequencies, different angle and different phase. Here the different frequencies between the image of SLM grating pattern and the sensor grating pattern are associated with the linear displacement on the optical axis z. The different angles between them depend on the angular displacement on roll angle. The different phase between them are associated with the linear displacements on the axis x and y. The three cases above are easily visible. However, the case that pitch (yaw) angular displacements as complex transformation is related to all of the frequency, the angle and the phase, is difficult to analyze the relation between the moiré fringe distribution and pitch angle(yaw angle). In the present paper, a special pattern called 5-grating pattern is designed to display in the DMD plane and the CCD plane. Two gratings with the same frequency in x-axis direction are respectively placed in the top and bottom of the pattern; two gratings with the same frequency in y-axis direction are respectively placed in the left and right of the pattern; and a square-ring grating is placed in the center of the pattern. By analyzing the geometric constraint and the imaging constraint on the object-image conjugate architecture, the differential phase between the top moiré fringe and the bottom moiré fringe is proposed to determine the pitch angular displacement, and the differential phase between the left moiré fringe and the right moiré fringe is proposed to determine the yaw angular displacement.

This paper presented here is aimed at solving the pixel-to-pixel alignment problem in computational photography by analyzing the relation between the moiré fringe distribution and six DoF displacements between the sensor and the based on 5-grating pattern. Its outline is as follows: The sum representation of Fourier-series decomposition corresponding to repetitive structures is introduced in Section 2. Whereafter, the moiré fringe distribution variations with the six DoF motions are deduced in Section 3. Pixel-to-pixel alignment method are described in Section 4, and the result and discussion are presented in Section 5. Finally, our paper is concluded in Section 6.

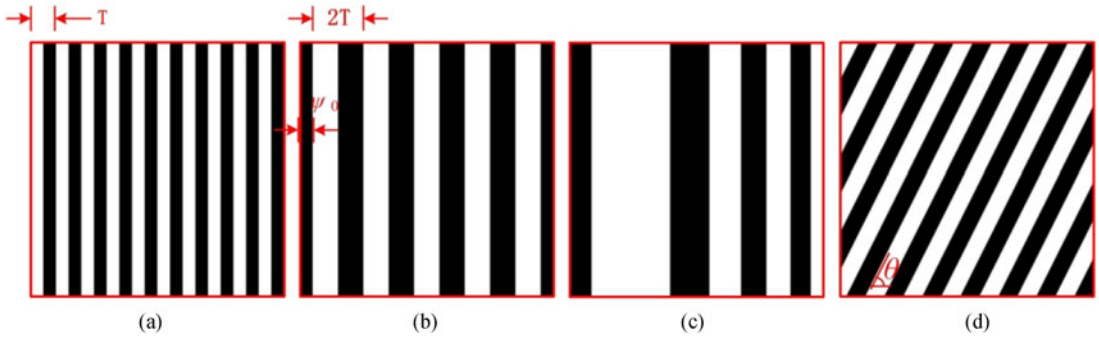

Fig. 1. Several representative repetitive grating: (a) standard rectangular grating with standardized period T, (b) linear transformation grating: $G(x, y) = x/2 - \psi_0$, (c) quadratic transformation grating: $G(x, y) = ax^2 + bx + c$, (d) rotated grating with the tilt angle θ: $G(x, y) = 2x + y$.

2. Fundamental Theory

2.1 Repetitive Structures

Repetitive structures are the basic elements which produce the moiré fringe phenomenon. In addition to the period structures, the quasi-period structures which can be obtained from a period structure by applying an appropriate spatial coordinate transformation are also classified as the repetitive structures in this paper. We analyze the repetitive structures to explore some beneficial properties as the theoretical basis of the latter deduction.

For the sake of simplicity, we begin with the simplest onefold periodic rectangular grating in 2D pattern. The element profile of the periodic rectangular grating is the rectangular pulse. It is well known that the distribution of complex amplitude of standard rectangular grating can be represented by an accumulation of complex exponential Fourier series with multiple frequencies according to the Fourier theory [11]. Assume that the fundamental period vector of standard rectangular grating is located on the x axis, the distribution of complex amplitude of standard rectangular grating can be expressed as:

$$E(x', y') = \sum_{n=-\infty}^{+\infty} c_n \exp(i2\pi n f x') \tag{1}$$

Where $f = 1/T$ is spatial repetitive frequency, and T is the fundamental period. c_n as Fourier coefficient of the rectangular function can be given by the following equation:

$$c_n = \frac{1}{T} \int_{-T/2}^{T/2} E(x', y') \exp(-i2\pi n f x') dx' \tag{2}$$

On the basis, other repetitive grating can be considered as extended coordinate-transformed results of original rectangular grating. Assume that the transformation function is denoted by $G(x, y)$, and the variable x' of the original rectangular grating can be replaced by the transformation function $G(x, y)$. The transformed repetitive grating can be obtained by this way:

$$E(x, y) = E[G(x, y)] = \sum_{n=-\infty}^{+\infty} c_n \exp[i2\pi n f G(x, y)] \tag{3}$$

A transformed repetitive grating is therefore characterized by the following properties:

The transformation function $G(x, y)$ is a mapping from the transformed coordinates to the original coordinates. The transformation will change the frequency, the angle and the phase of the rectangular grating throughout the plane. In the case that the transformation function is a linear equation in one unknown, the transformed grating is only different from original grating in the spatial frequency constant and the initial phase ψ_0, as is shown in Fig. 1(b). In the case of quadratic or higher equation in one unknown, the spatial frequency is a variable along x-axis or y-axis. As a example,

parabolic equation $ax^2 + bx + c = x'$ is shown in Fig. 1(c). Fig. 1(d) shows the case of the linear equation in two unknowns that the original grating changes to a rotated grating with the variation of the frequency and the angle θ. In the case of quadratic or higher equation in two unknowns, The periodic profiles of the transformed gratings appear to be circular shape, elliptical shape, parabola shape and other complex shapes, as discussed in [11].

2.2 Superposed Moiré Fringe Distribution

We can express multiple grating superposition as a product of the amplitude distributions of the individual gratings. According to the actual application in this paper, the case of double grating superposition is only discussed. Assume that two repetitive grating which are transformed from two original rectangular grating with initial frequency f_1 and f_2. $G_1(x, y)$ and $G_2(x, y)$ denote their respective transformation function. Hence, the transformed repetitive grating can be respectively given

$$E_1(x, y) = \sum_{n=-\infty}^{+\infty} c_n \exp\left[i2\pi n f_1 G_1(x, y)\right] \tag{4}$$

$$E_2(x, y) = \sum_{m=-\infty}^{+\infty} c_m \exp\left[i2\pi m f_2 G_2(x, y)\right] \tag{5}$$

Where, $G_1(x, y)$ and $G_2(x, y)$ generally involve the frequency component, the angle component and the phase component. However, when the frequency being separately analyzed, the frequency components of transformation functions can be incorporated in f_1 and f_2. Likewise, in the case of making a separate analysis of angle component, we can choose a normalized frequency to be $f = 1$ and incorporate the angle components of transformation functions into the Fourier coefficients c_n and c_m.

Thus the distribution of the double grating superposition is expressed as

$$\begin{aligned} E(x, y) &= E_1(x, y)E_2(x, y) \\ &= \left\{\sum_{n=-\infty}^{+\infty} c_n \exp\left[i2\pi n f_1 G_1(x, y)\right]\right\} \times \left\{\sum_{m=-\infty}^{+\infty} c_m \exp\left[i2\pi m f_2 G_2(x, y)\right]\right\} \\ &= \sum_{n=-\infty}^{+\infty}\sum_{m=-\infty}^{+\infty} c_n c_m \exp\left\{i2\pi[n f_1 G_1(x, y) + m f_2 G_2(x, y)]\right\} \end{aligned} \tag{6}$$

Here, Eq. (6) is a double sum function. By extracting the partial sum of Eq. (6), a new distribution similar to Eq. (3) will be obtained:

$$E_{n,m}(x, y) = \sum_{k=-\infty}^{+\infty} c_{kn} c_{km} \exp\left\{i2\pi k f[n G_1(x, y) f_1/f + m G_2(x, y) f_2/f]\right\} \tag{7}$$

Here, $G(x, y) = nG_1(x, y)f_1/f + mG_2(x, y)f_2/f$ can be regarded as the transformation function of a original grating with initial frequency *f*. The new distribution which appears as a repetitive layout with white and black pattern is moiré fringe. Where n and m are the integers except 0. The term (n, m) is named as the order of the moiré. By assigning the term (n, m), the partial sums corresponding to each order moiré will be obtained. Whether a certain moiré is visible or not depends on the condition that its amplitude is stronger than the sensitivity of sensor and the effective period (i.e., the reciprocal of frequency) is greater than the resolution of sensor. This has been discussed in detail in [21]. Due to frequencies of two gratings for the pixel-to-pixel alignment application being in close proximity to each other, the (1, −1) moiré or the (−1,1) moiré is the optimal order in which its frequency is the smallest and its amplitude is the strongest. We take the (1, −1) moiré to analyze the relation between the SLM and the sensor in this paper. Thus, the visible moiré can

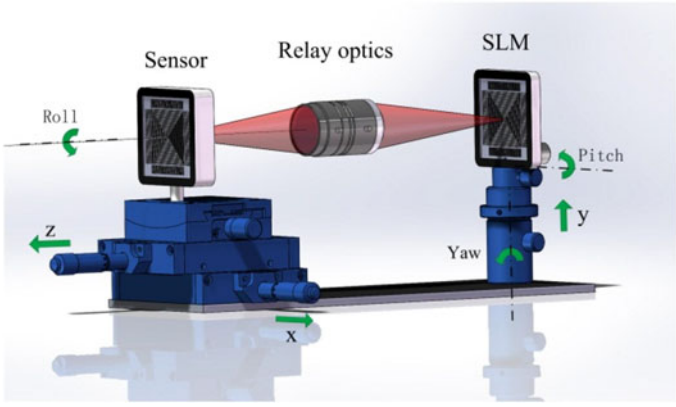

Fig. 2. Schematic of optical arrangement with 6-axis stages.

be expressed as

$$E_{1,-1}(x, y) = \sum_{k=-\infty}^{+\infty} c_k c_{-k} \exp\left\{i2\pi kf[G_1(x, y)f_1/f - G_2(x, y)f_2/f]\right\} \tag{8}$$

Some results about the superposed moiré fringe distribution can be therefore formulated as the follows:

The moiré fringe produced by the superposition of two repetitive structures is equivalent to the result into which arbitrary original grating with initial frequency f can be transformed by a certain transformation function. In addition, every moiré fringe can be represented by the partial sum of Fourier-series decomposition of two grating superposition. In our application, the fringe visibility of the (1, −1) moiré and the (−1, 1) moiré are the highest one among all (n, m) moiré orders.

3. Moiré Fringe Distribution Variations

In computational photography, the SLM as one grating is imaged on the sensor as another grating with relay optics, that is, the sensor and the SLM are mutually object-image conjugate. Fig. 2 is the schematic of optical arrangement. The displacements between the SLM and the sensor are adjustable in six axes. The purpose of this section is to analyze the moiré fringe distribution variations with the six DoF motions, and to propose the method for pixel-to-pixel alignment.

3.1 Linear Displacement on the Optical Axis z

In the theory of geometrical optics, vertical magnification of two conjugate plane in the paraxial zone depends on the linear displacement in optical axis z between the sensor plane and the SLM plane when the focal length of relay optics is given. Sizes of the sensor and the SLM off the shelf are priori known, that is, spatial periods of the two gratings are constant. Hence, vertical magnification caused by the linear displacement on the optical axis z determines the frequency difference between the sensor grating and the SLM grating. Regardless of other factors about angles and phases, the distribution of the (1, −1) moiré produced by the two superposed gratings with the same transformation function $G(x, y)$ can be expressed as

$$E_{1,-1}(x, y) = \sum_{k=-\infty}^{+\infty} c_k c_{-k} \exp\left\{i2\pi k(f_1 - f_2)G(x, y)\right\} \tag{9}$$

Where f_1 is the frequency of the sensor grating, and f_2 is the frequency of the SLM grating magnified by relay optics. $G(x, y)$ refer to the same transformation function of two original rectangular gratings. For conveniently controlling frequency difference, we choose x or y as the transformation

function $G(x, y)$. By substituting $G(x, y) = x$ into Eq. (9), the distribution of the (1, −1) moiré can be rewritten as

$$E_{1,-1}(x, y) = \sum_{k=-\infty}^{+\infty} c_k c_{-k} \exp\left[i2\pi kx(f_1 - f_2)\right] \tag{10}$$

As Eq. (10) indicates, we can obtain the following deduction: The orientation of the moiré fringe is identical to those of two original gratings. The repetitive period of the moiré fringe is longer than $1/f_1$ and $1/f_2$. By adjusting vertical magnification of imaging system to be $f_1 = f_2$, the moiré fringe will be disappearing. Therefore, in the case of the linear displacement in optical axis z between the sensor plane and the SLM plane, the pixel-to-pixel alignment can be accomplished by disappearing the moiré fringe.

3.2 Angular Displacement on Roll Angle

The angular displacement on roll angle between the sensor plane and SLM plane will generate the rotational transformation of the coordinate system. Regardless of other DoF factors, i.e., the frequency of the SLM grating is identical to the frequency of the sensor grating $f_1 = f_2 = f$, the distribution of the (1, −1) moiré produced by the two superposed gratings with the same frequency f can be expressed as

$$E_{1,-1}(x, y) = \sum_{k=-\infty}^{+\infty} c_k c_{-k} \exp\left\{i2\pi kf[G_1(x, y) - G_2(x, y)]\right\} \tag{11}$$

Where $G_1(x, y)$ and $G_2(x, y)$ as only rotational transformation with rotational angle θ_1 and θ_2 can be respectively represented by $G_1(x, y) = x\cos\theta_1 - y\sin\theta_1$ and $G_2(x, y) = x\cos\theta_2 - y\sin\theta_2$. The frequency of the produced moiré is a new impulse amplitude rather than f.

In the case of taking special value $\theta_2 = 0$ on the rotational angle of the sensor grating, the rotational angle θ_1 of the SLM grating is equal to the angle difference θ between them. The distribution of the (1, −1) moiré can be rewritten as

$$\begin{aligned} E_{1,-1}(x, y) &= \sum_{k=-\infty}^{+\infty} c_k c_{-k} \exp\left\{i2\pi kf[x\cos\theta - y\sin\theta - x]\right\} \\ &= \sum_{k=-\infty}^{+\infty} c_k c_{-k} \exp\left\{i2\pi kf\sqrt{2 - 2\cos\theta}\left[x\frac{\cos\theta - 1}{\sqrt{2 - 2\cos\theta}} - y\frac{\sin\theta}{\sqrt{2 - 2\cos\theta}}\right]\right\} \end{aligned} \tag{12}$$

Where $f\sqrt{2 - 2\cos\theta}$ denotes the frequency of the produced moiré f_m. The orientational angle θ_m of the produced moiré conforms to the formula: $\tan\theta_m = \sin\theta/(\cos\theta - 1)$.

As Eqs. (11)–(12) indicate, we can obtain the following deduction: With the diminution of the angular displacement on roll angle between the sensor plane and the SLM plane, the frequency f_m of the produced moiré will gradually decrease, and the orientational angle θ_m will be perpendicular to the orientation of the two original gratings. By diminishing the angle difference θ to be $G_1(x, y) = G_2(x, y)$, the moiré fringe will be disappearing. Therefore, in the case of the angular displacement on roll angle between the sensor plane and SLM plane, the pixel-to-pixel alignment can be also accomplished by disappearing the moiré fringe.

3.3 Linear Displacements on the Axis x and y

The linear displacement on the axis x or y will give rise to the phase variation of the SLM grating and the sensor grating. Assuming that the frequencies of the two grating without the orientational transformation are identical, the distribution characteristic of the superposed pattern is more obvious by geometric analysis in spatial domain. As shown in Fig. 3, the intensity distribution of the SLM

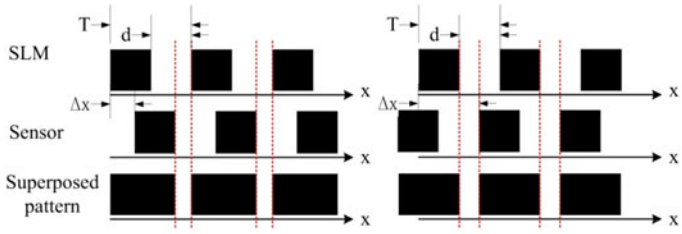

Fig. 3. The geometric analysis in spatial domain.

rectangular grating and the sensor rectangular grating are expressed as

$$E_1(x, y) = \sum_{n=-\infty}^{+\infty} \text{rect}\left(\frac{x - nT}{d}\right) \tag{13}$$

$$E_2(x, y) = \sum_{m=-\infty}^{+\infty} \text{rect}\left(\frac{x - mT - \Delta x}{d}\right) \tag{14}$$

Where Δx denotes the linear displacement of the SLM grating and the sensor grating. d as the width of rectangular pulse is equal to $T/2$ in our application. The distribution characteristic of the superposed pattern caused by the phase variation in one period is yielded in this following:

$$E(x, y) = E_1(x, y)E_2(x, y) = \begin{cases} \sum_{k=-\infty}^{+\infty} \text{rect}\left(\frac{x-kT-\Delta x/2}{T/2-\Delta x}\right) & 0 \le \Delta x < T/2 \\ \sum_{k=-\infty}^{+\infty} \text{rect}\left(\frac{x-kT+T/2-\Delta x/2}{\Delta x-T/2}\right) & T/2 \le \Delta x < T \end{cases} \tag{15}$$

As Eq. (15) indicate, we can obtain the following: The superposed pattern caused by the phase variation is a new periodic rectangular fringe. The linear displacement in axis x changes the periodic profile of the superposed pattern which is really not the moiré fringe. In the case of that the linear displacement $\Delta x = (n + 1/2)T$, the superposed periodic rectangular fringe will be disappeared. We can regard this moment as the mark that the pixel-to-pixel alignment is accomplished.

3.4 Pitch and Yaw Angular Displacements

Compared to other displacements, pitch and yaw angular displacements will give rise to the complex transformation including the frequency, the angle and the phase. For obtaining the transformation function, the geometric constraint and the imaging constraint affecting coordinate transformation will be respectively analyzed. Fig. 4 shows the relation between the yaw angular displacement and the x-axis coordinate transformation. Yaw angular displacement φ as the geometric factor narrows the period of the SLM grating. This part of the coordinate transformation actually is the orthogonal projection of x on the reference plane. The projection transformation is expressed as

$$t_p(x, y) = x \cos\varphi \tag{16}$$

Because the sensor plane and the reference plane are mutually object-image conjugate, the axial displacement $x \sin\varphi$ caused by yaw angular displacement changes the ratio of the vertical magnification. Assuming that the frequency ratio of the sensor grating to the SLM grating on the reference plane is 1, the ratio of the vertical magnification $\beta(x, y)$ will change to be $\beta(x, y) = 1 + x \sin\varphi/F$ according to Newton's image-formation formula after the rotation of the SLM on roll angle. Here F is the focal length in the image space. Total coordinate transformation $G_t(x, y)$ affected by the geometric constraint and the imaging constraint yields the product of the projection

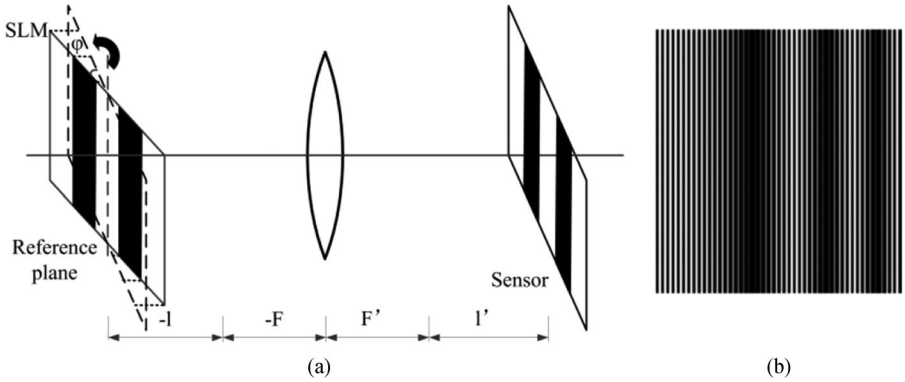

Fig. 4. The relation between the yaw angular displacement and x-axis coordinate transformation: (a) the geometric constraint and the imaging constraint caused by yaw angular displacement. (b) the simulate pattern.

transformation and the ratio of the vertical magnification, that is to say:

$$G_t(x, y) = t_p(x, y)\beta(x, y) = x\cos\varphi(1 + x\sin\varphi/F) \tag{17}$$

On the basic of theory in Section 2, by substituting Eq. (17) into Eq. (8), the moiré fringe produced by the superposition of the sensor pattern and the SLM pattern after coordinate transformation can be expressed as

$$\begin{aligned} E_{1,-1}(x, y) &= \sum_{k=-\infty}^{+\infty} c_k c_{-k} \exp\left\{i2\pi kf[x\cos\varphi(1 + x\sin\varphi/F) - x]\right\} \\ &= \sum_{k=-\infty}^{+\infty} c_k c_{-k} \exp\left\{i2\pi kf[(\cos\varphi\sin\varphi/F)x^2 + (\cos\varphi - 1)x]\right\} \end{aligned} \tag{18}$$

Thus it can be seen that the superposed moiré fringe distribution is equivalent to the parabolic transformation of the original rectangular grating. The simulate pattern is shown in Fig. 4. Thus we can obtain the yaw angular displacement φ based on the superposed moiré fringe distribution. With the yaw angular displacement φ diminishing, the parabolic moiré fringe will move to the direction of axial displacement increasement, and fringe number will decrease. Until the parabolic moiré fringe is disappeared, the pixel-to-pixel alignment between the sensor and SLM will be not accomplished. We can process the case of pitch angular displacement in a similar way. Based on the above theory, the case that pitch and yaw angular displacements together give rise to the moiré fringe transformation is discussed in the next section.

4. Pixel-to-Pixel Alignment

4.1 Experimental Setup

For verifying the theory above and summarizing accurate pixel-to-pixel alignment method, we construct a experimental setup composed of CCD, DMD, relay lens, and 6-Axis Stages. Fig. 5 shows the arrangement of the experimental setup. Here the CCD as the sensor allows for 8 bits per pixel (bpp) of precision in the RAW mode and a resolution of 768 $\times$ 576; each pixel of CCD is 7.4 $\times$ 7.4 μm^2 in size. The DMD as the SLM provides 8 bpp and a resolution of 1140 $\times$ 912; each mirror element is 7.6 $\times$ 7.6 μm^2. The vertical magnification of relay lens is adjustable in the range from 0.3 to 3.5; the focal length in the image space is approximately 100 mm. The DMD is mounted on a 3-Axis adjuster including yaw axis, pitch axis and the y-axis. And the CCD is mounted on a 3-Axis assembled stage offering the high precise travel on roll axis, the x-axis and the z-axis. The experimental setup as a main component is widespread in most of computational imaging devices.

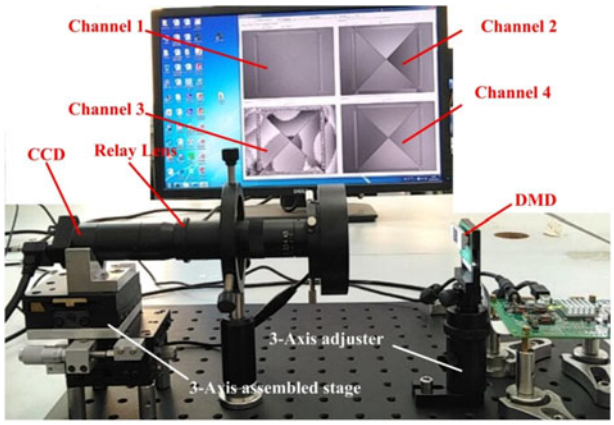

Fig. 5. The arrangement of the experimental setup.

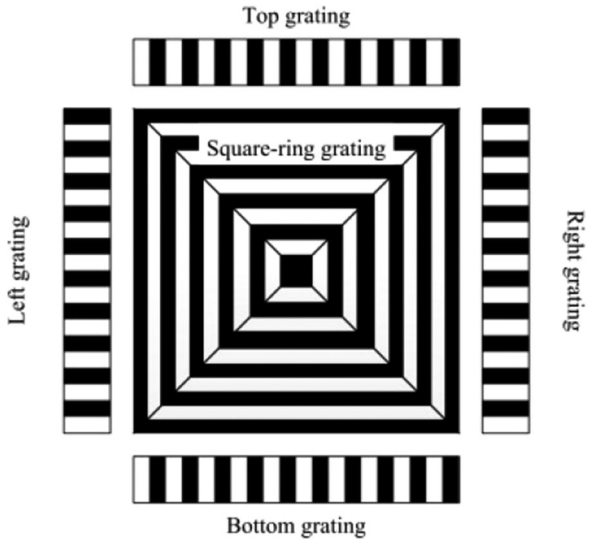

Fig. 6. 5-grating pattern.

In addition, a display device is used to monitor the superposed pattern which the CCD captures in real time. The screen is composed of the original image in channel 1, the moiré fringe image in channel 2, the phase distribution image in channel 3 and the profile-varying periodic fringe image in channel 4. The original image in channel 1 is the DMD grating pattern is captured by CCD. The moiré fringe image in channel 2 is acquired by a subsampling operation on the original image. The phase distribution image in channel 3 is calculated from the moiré fringe image. The profile-varying periodic fringe image in channel 4 is acquired by neighbor interpolation operation on the moiré fringe image.

In the process that the DMD plane is imaged onto the CCD plane with relay lens, a desirable outcome is to achieve pixel-to-pixel correspondence. Note that there are three possibilities for the mapping from the DMD to the CCD: one DMD pixel being assigned to multiple CCD pixels, one DMD pixel being assigned to one CCD pixel, and multiple DMD pixels being assigned to one CCD pixel. The mapping of one DMD pixel being assigned to one CCD pixel is taken for example in this paper. (Same method can be also used for the other two mappings.) To achieve the pixel-to-pixel alignment based on moiré fringe theory in Section 2 and 3, a special grating pattern composed of 5 different gratings is designed to display in the DMD plane and the CCD plane. As is shown in Fig. 6, two gratings with the same frequency in x-axis direction are respectively placed in the top

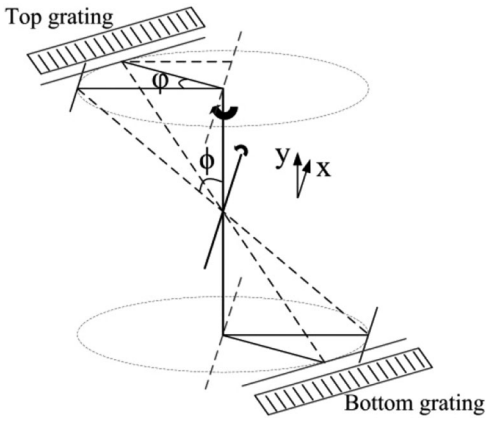

Fig. 7. The geometrical transformation diagram of the top and bottom gratings.

and bottom of the pattern; two gratings with the same frequency in y-axis direction are respectively placed in the left and right of the pattern; and a square-ring grating is placed in the center of the pattern. In the next experiment, we choose the fundamental period to be T = 4 pixels, and the width of rectangular pulse to be d = 2.

4.2 Alignment Procedure

In the actual experiment, six DoF factors collectively affect the fringe distribution of 5-grating pattern rather than separately. Therefore the theory in Section 3 does not simply apply to the pixel-to-pixel alignment. Based on the fringe characteristics which is specialized for 5-grating pattern, our alignment procedure is described as follows:

Step 1 Eliminate the roll angular displacement. Roll angle is not associated with yaw angle and pitch angle in Eulerian coordinate. In case of the small frequency difference between the CCD grating and the DMD grating, the frequency f_m and the orientational angle θ_m can be yielded in a similar way to Section 3.2:

$$f_m = \sqrt{{f_1}^2 + {f_2}^2 - 2f_1 f_2 \cos(\theta_1 - \theta_2)} \tag{19}$$

$$\theta_m = \arccos[(f_1 \cos\theta_1 - f_2 \cos\theta_2)/f_m] \tag{20}$$

Where f_1 and f_2 denote the frequencies of the CCD grating and the DMD imaging grating respectively. θ_1 and θ_2 are the rotational angles of them respectively. With the diminution of the roll angular displacement, the orientational angle θ_m will be gradually parallel to the original grating fringe, and the frequency f_m will be gradually decrease to the frequency difference in the process. In addition to the characteristics above, cross lines can assist in judging whether the roll angular displacement is zero. Fig. 9 show the process of the step 1 that the roll angular displacement is eliminated by monitoring the frequency f_m and the orientational angle θ_m of the moiré fringe vector in square-ring grating pattern of channel 2.

Step 2 Eliminate the yaw angular displacement and the pitch angular displacement. With respect to the original grating fringe vector along the x-axis, the geometric factor $t_{p,x}(x, y) = x\cos\varphi$ caused by the yaw angular displacement is not associated with the pitch angular displacement. Likewise, with respect to the original grating fringe vector along the y-axis, the geometric factor $t_{p,y}(x, y) = y\cos\phi$ caused by the pitch angular displacement is not associated with the yaw angular displacement. However, the ratios of the vertical magnification $\beta(x, y)$ are associated with the yaw angular displacement and the pitch angular displacement. Fig. 7 shows the axial displacement distribution on the top grating and bottom grating caused by the yaw angular displacement and the pitch angular displacement. According to the imaging constraint formula in Section 3.4, we can

obtain the ratios of the vertical magnification:

$$\beta_x(x, y) = [(y \sin\phi + b)\cos\varphi - (x + a)\sin\varphi]/F + 1 \tag{21}$$

Where a denotes the distance between the yaw axis and y-axis, and b denotes the distance between the pitch axis and x-axis. According to Eq. (17), total coordinate transformation can be rewritten as:

$$G_t(x, y) = \left\{[(y \sin\phi + b)\cos\varphi - (x + a)\sin\varphi]/F + 1\right\} \cdot x\cos\varphi \cdot \eta \tag{22}$$

Where η denotes the frequency ratio of the CCD grating to the DMD grating in the reference plane.

The moiré fringe produced by the superposition of the CCD grating and the DMD grating can be expressed as

$$E_{1,-1}(x, y) = \sum_{k=-\infty}^{+\infty} c_k c_{-k} \exp\left\{i2\pi kf\left[-\frac{\eta}{F}\sin\varphi\cos\varphi \cdot x^2 + \lambda(y) \cdot x - \omega_x\right]\right\} \tag{23}$$

Where $\lambda(y) = \{[(y \sin\phi + b)\cos\varphi - a\sin\varphi + F]\cos\varphi \cdot \eta/F - 1\}$ is a linear function with respect to y. ω_x denotes the initial phase of the moiré fringe along the x-axis.

As Eq. (23) indicates, we can obtain that the superposed product of the CCD grating and the DMD grating is still a parabolic moiré fringe. However, yaw angle φ and pitch angle ϕ are both small, so the quadratic term of transformation function is slim relative to the linear term. It makes the difficulty in extracting the distribution feature of the parabolic moiré fringe. In addition, it is also difficult to determine the coordinates of the yaw axis and pitch axis in x-y plane. To avoid the problem above, the differential phase between the top moiré fringe and the bottom moiré fringe is employed in the process of eliminating the pitch angular displacement. Assuming that y_1 and y_2 are respectively the ordinate values of the top moiré fringe and the bottom moiré fringe after step 1, the difference between the top moiré fringe and the bottom moiré fringe can be expressed as

$$\lambda(y_1) - \lambda(y_2) = (y_1 - y_2)\sin\phi\cos^2\varphi \cdot \eta/F \tag{24}$$

The differential phase m between the two parabolic moiré fringe can be obtained by

$$m = \frac{(y_2 - y_1)\sin\phi\cos^2\varphi \cdot \eta/F}{2\sin\varphi\cos\varphi \cdot \eta/F} = \frac{(y_2 - y_1)\sin\phi}{2\tan\varphi} \tag{25}$$

In a similar way, the differential phase n between the left moiré fringe and the right moiré fringe can be obtained by

$$n = \frac{(x_2 - x_1)\sin\varphi\cos^2\phi \cdot \eta/F}{2\sin\phi\cos\phi \cdot \eta/F} = \frac{(x_2 - x_1)\sin\varphi}{2\tan\phi} \tag{26}$$

By this means, a, b, η and F are cancelled. The complex problem is simplified as the differential phase monitor in channel 2. Fig. 9 show the process of the step 2 that the yaw and pitch angular displacement are eliminated by adjusting the differential phase n and m to zero.

Step 3 Adjust the linear displacement on the optical axis z. After the step 1 and 2, the frequency difference caused by the linear displacement on optical axis z plays a dominant role in moiré fringe distribution. The characteristic of moiré fringe distribution has been discussed in Section 3.1. In global pattern of channel 2, the frequency difference is reflected as the stripe number. The less the stripe number is, the smaller the frequency difference is. To implement pixel-to-pixel adjustment more accurate, the phase distribution is analyzed after the last stripe has been disappeared. The phase distribution image in channel 3 can be obtained by the N-step phase-shifting algorithm, as described in detail in [5]. We regard the uniform phase distribution as the mark that the frequency ratio of the CCD grating to the DMD grating is equal to 1. Fig. 9 show the process of the step 3 that the frequency difference is eliminated.

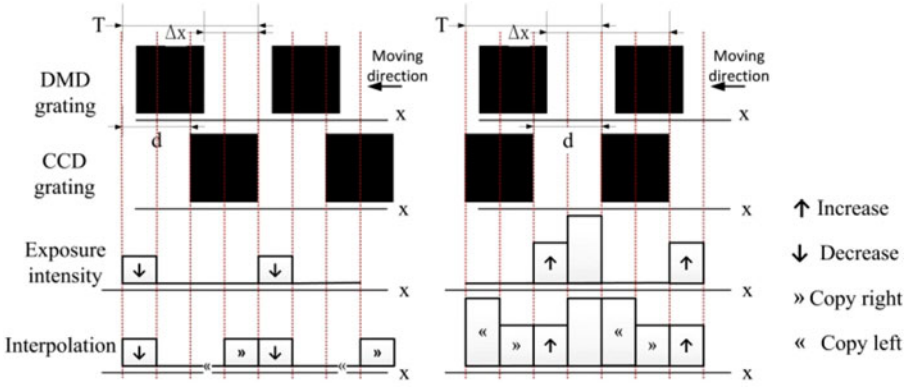

Fig. 8. The schematic of step 4.

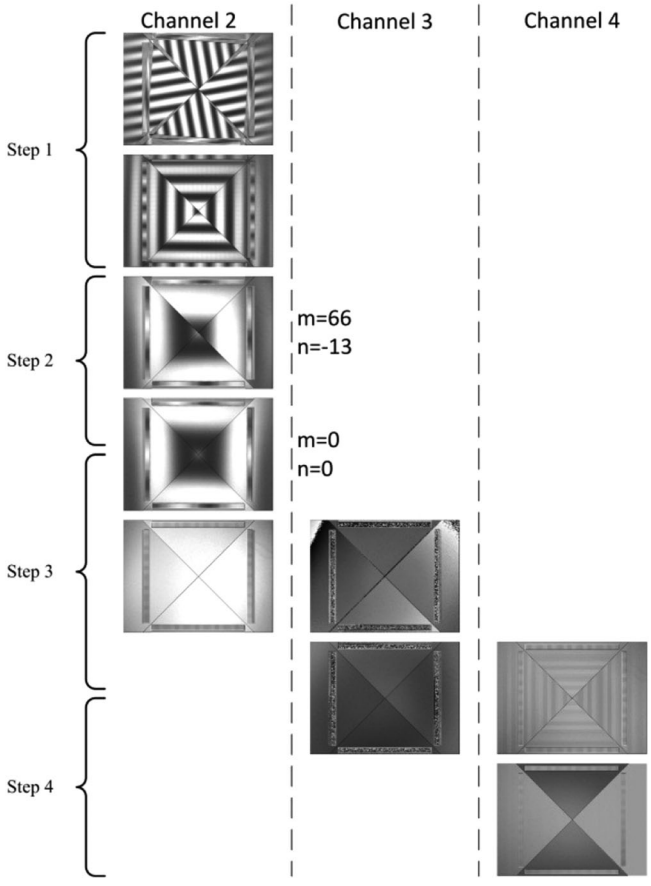

Fig. 9. Alignment Procedure.

Step 4 Adjust the linear displacement on the axis x and y. Fig. 8 shows the generating principle of the profile-varying periodic fringe image in channel 4. The linear displacement on the x-axis or the y-axis change the periodic profile of the superposed pattern to a new periodic rectangular fringe according to the Section 3.3. After the CCD samples the new periodic rectangular fringe, the periodic profile occurs secondary change. The two pixels of rectangular trough in channel 4 are interpolated using their neighboring sampled pixels respectively. To observe the variation of the

periodic profile clearer, two cases in Fig. 8 are both applied to the square-ring grating. With the CCD grating shifting on x-axis or y-axis, visibility of fringe is varied periodically in channel 4. At the moment that the periodic fringes in the area of square-ring grating are disappeared, pixel-to-pixel alignment has been accomplished, as shown in the step 4 of Fig. 9.

5. Discussion on the Alignment Accuracy

Here, the accuracy of every step in the alignment procedure above is discussed. The moiré fringe vector is monitored to adjust the roll angular displacement in step 1. The error of the roll angular displacement observed is associated with orientational angle θ_m of the moiré fringe. For the sake of simplicity, the DMD grating vector is chosen to be unit vector in x-axis. By substituting the CCD grating vector $\overrightarrow{f_1} = (\eta \cos\theta_1, \eta \sin\theta_1)$ and the DMD grating vector $\overrightarrow{f_2} = (1, 0)$ into Eqs. (19), (20), the orientational angle θ_m of the moiré fringe is derived as

$$\sin\theta_m = \sin\theta_1 \cdot \eta / \sqrt{\eta^2 + 1 - 2\eta\cos\theta_1} \tag{27}$$

By taking the differential on both side of Eq. (27), we can obtain the following equation:

$$\cos\theta_m \cdot d\theta_m = \left(\eta / \sqrt{\eta^2 + 1 - 2\eta\cos\theta_1}\right) \cdot d\theta_1 \tag{28}$$

When the terms $d\theta_m$ and $d\theta_1$ can be replaced by the angle errors $\Delta\theta_m$ and $\Delta\theta_1$, and the angles θ_m and θ_1 are close to zero, Eq. (28) can be rewritten as:

$$\Delta\theta_1 = [(\eta - 1)/\eta] \cdot \Delta\theta_m \tag{29}$$

Where $\Delta\theta_m$ is determined by the size of 5-grating pattern in pixel coordinate. In our experiment, the angle error of the moiré fringe $\Delta\theta_m$ is smaller than 1/480. η spread over the range from 401/400 to 404/400 after the coarse adjustment. Hence, the error of the roll angular displacement $\Delta\theta_1 < 10^{-4}$ is small enough to ignore after step 1.

The differential phase *n* and *m* are monitored to adjust the yaw and pitch angular displacement in step 2. The relation between the differential phase and the yaw and pitch angular displacement is given by Eqs. (25), (26). By taking the differential on both side of Eqs. (25), (26) respectively, we can obtain the following equations:

$$dm = [(y_2 - y_1)\cos\phi/(2\tan\varphi)] \cdot d\phi \tag{30}$$

$$\mathrm{dn} = [(x_2 - x_1)\cos\varphi/(2\tan\phi)] \cdot d\varphi \tag{31}$$

By substituting $\cos\phi \approx 1$ and $\cos\varphi \approx 1$ into Eqs. (30), (31), the errors of the yaw and pitch angular displacement can be expressed as

$$\Delta\varphi = [2\tan\phi/(x_2 - x_1)] \cdot \Delta n \tag{32}$$

$$\Delta\phi = [2\tan\varphi/(y_2 - y_1)] \cdot \Delta m \tag{33}$$

Where Δn and Δm denote the quantization errors of the sampling differential phase, as are suggested to be 1 in pixel coordinate. The difference between the top moiré fringe and the bottom moiré fringe on the y-axis is 440 pixels, the same as the difference between the left moiré fringe and the right moiré fringe on the x-axis. For $\sin\phi$ and $\sin\varphi$, ϕ and φ spread over the range from 0 to 1° after the coarse adjustment. Hence, the errors of the yaw and pitch angular displacement $\Delta\varphi < 10^{-4}$ and $\Delta\phi < 10^{-4}$ are small enough to ignore after step 2.

The phase distribution of the moiré fringe is monitored to adjust the frequency difference between the CCD grating and the DMD grating in step 3. As Fig. 10 shows, the angular frequency can be determined by the phase distribution of the moiré fringe. The case of Fig. 10(b) is the optimal performance in our experiment. Fig. 10(c) and Fig. 10(d) are respectively the phase distribution of the moiré fringe in the y directional section in red line of Fig. 10(a) and Fig. 10(b). The angular

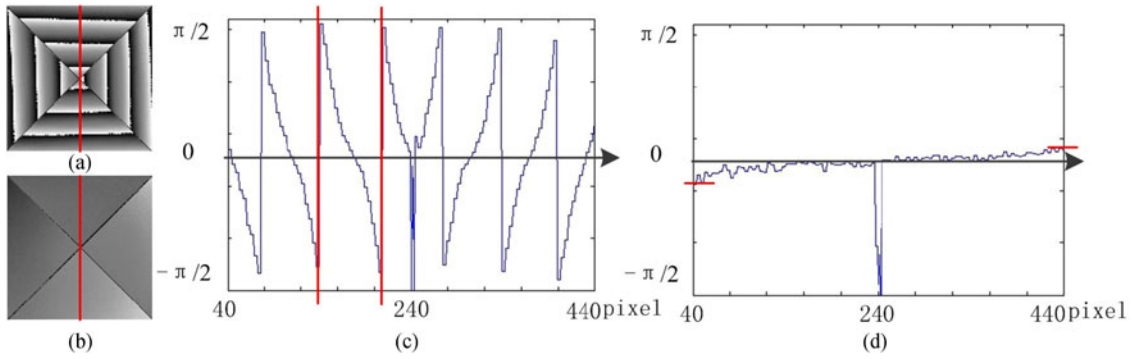

Fig. 10. The phase distribution of the moiré fringe in step 3: (a) the phase distribution image in channel 3 before adjustment, (b) the phase distribution image in channel 3 after adjustment, (c) the phase distribution of the moiré fringe in the y directional section in red line of Fig. 10(a), (d) the phase distribution of the moiré fringe in the y directional section in red line of Fig. 10(b).

frequency ω can be expressed as the phase difference per pixel on the y-axis:

$$\omega = \Delta\psi/\Delta L \tag{34}$$

Here ΔL denotes the spatial distance with respect to the phase difference $\Delta\psi$

Thus the frequency of the moiré fringe, i.e., the frequency difference between the CCD grating and the DMD grating, can be given by the following equation:

$$\Delta f = f_m = \Delta\psi/(2\pi \cdot \Delta L) \tag{35}$$

In the case of Fig. 10(c), the error of the frequency difference between the CCD grating and the DMD grating is $1/130(pixel^{-1})$. With adjusting the linear displacement on the optical axis z, the error of the frequency difference is reduced to $1/8000(pixel^{-1})$ in Fig. 10(d).

The periodic profile of the new rectangular fringe is monitored to adjust the linear displacements Δx and Δy in step 4. The large number of periodic profiles can be evaluated by envelopes in statistical analysis theory. As Fig. 3 indicates, the relation between the amplitude difference of envelopes ΔI and the linear displacement Δx is expressed as:

$$(d - \Delta x)/d = \Delta I / I_{\max} \tag{36}$$

Here, $I_{\max}$ denotes the maximal amplitude. Fig. 11 is the experimental datum and analysis in step 4. Fig. 11(a) and Fig. 11(b) are the profile-varying periodic fringe images with respect to different linear displacements. Fig. 11(c) and Fig. 11(d) are respectively the envelope curves of image intensity in the y directional section in red line of Fig. 11(a) and Fig. 11(b). Fig. 11(b) is the optimal performance in our experiment. In the case of Fig. 11(b), The error of the linear displacement $\Delta\chi$ between the CCD pixel and the DMD pixel is 1.95%.

Considering the errors of the frequency difference and the linear displacement, we can obtain the error of the aligned pixel square (or alignment error) by the following equation:

$$\Delta S = (\partial S/\partial f) \cdot \Delta f + (\partial S/\partial \chi)\Delta\chi \tag{37}$$

Where the aligned pixel square is obtain by $S = (1 - D \cdot f - \chi)^2$, and D is the pixel distance from the image center.

To verify the advantage in accuracy, our alignment method is compared with the three-step alignment method in [20] through experiment and error analysis. The results of these calculations are given in Table 1. The analyzed image size is 640 × 480 pixels. In three-step alignment method, regardless of the limitation on visual resolution, the straight form change of moiré fringe in one pixel size can be observed. The quantization error of the roll angular displacement is associated with the length of moiré fringe. Assuming that four quasi-periodic fringes in x/y axis are used to find out the

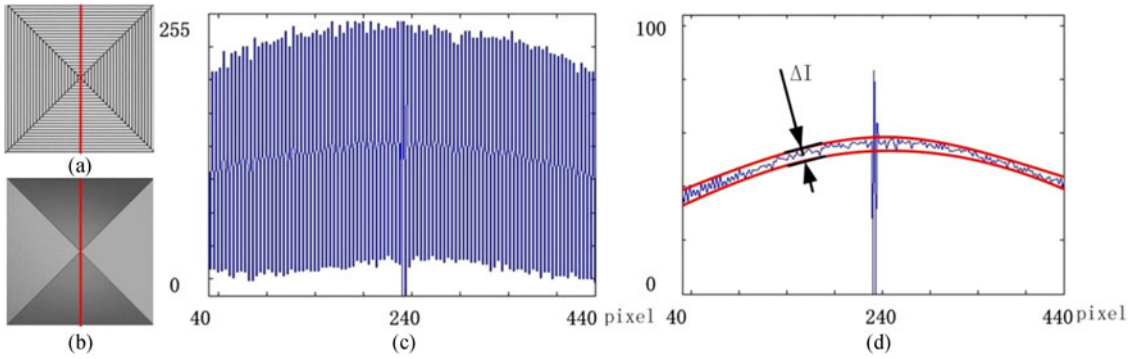

Fig. 11. The image intensity in step 4: (a) the profile-varying periodic fringe images in channel 4 before adjustment, (b) the profile-varying periodic fringe images in channel 4 after adjustment, (c) the envelope curves of image intensity in the y directional section in red line of Fig. 11(a), (d) the envelope curves of image intensity in the y directional section in red line of Fig. 11(b).

TABLE 1
Alignment Error of Two Methods

	$\Delta\theta_1$ (rad)	$\Delta\phi$, $\Delta\varphi$ (rad)	Δf (px^{-1})	Δx , Δy (px)	Alignment error (%)	
					maximum	mean
Three-step alignment	5.2×10^{-4}	8.3×10^{-3}	1.25×10^{-4}	0.0508	42.3	14.6
Proposed method	2.1×10^{-5}	7.9×10^{-5}	1.25×10^{-4}	0.0195	10.6	4.07

slight curvature change of moiré fringe, the quantization error of the pitch/yaw angular displacement is equal to 1/120. The initial phase in the phase distribution image is used to adjust the x and y displacement in three-step alignment method. The phase distribution curve is mixed with noise which amplitude is $\pi/20$, i.e., quantization error of initial phase is $\pi/20$, as shown in Fig. 10(d). The error of the linear displacement between the CCD pixel and the DMD pixel is equal to 5%. In our Proposed method, the relations between the moiré fringe distribution and six DoF displacements are analyzed respectively. The frequency f_m, the angles θ_m, the differential phase m and n, the amplitude difference of envelopes ΔI as quantized variables are automatically monitored. Errors of six DoF displacements are calculated by Eqs. (29), (32), (33), (35), (36). Alignment error in three-step alignment method is mainly derived from the roll, pitch and yaw angular errors. Our proposed method is better than three-step alignment method in the roll, pitch, yaw angular adjustments and the x-axis, y-axis linear adjustments. With the increase in the pixel distance from the image center, the alignment error will gradually grow larger. The maximal error of the aligned pixel square in global aligned area is 10.6%. For most of pixels, the accuracy of the pixel-to-pixel alignment can reach 90% above.

6. Conclusion

In this works, we described a pixel-to-pixel alignment method that utilizes 5-grating pattern to monitor and adjust the six DoF displacements step by step. Specially, the characteristics of the moiré fringe distribution variations caused by six DoF displacement were studied theoretically. On the basic of the theory, some quantized variables including the frequency f_m, the orientational angle θ_m, differential phase m & n, the frequency difference Δf and the amplitude difference of envelopes ΔI are employed to determine six DoF displacement. Compared with three-step alignment procedure, proposed method has obvious advantages in roll, pitch and yaw alignment precisions. Roll, pitch and yaw angular errors have a big influence on the pixel-to-pixel alignment accuracy on the side of

image. Furthermore, the amplitude difference of envelopes $\triangle I$ is a result of mean algorithm avoiding random noise disturbance in three-step alignment method. In short, the alignment accuracy was significantly improved by our proposed method.

The mapping of one DMD pixel being assigned to one CCD pixel is taken for example in this paper. If multiple DMD/CCD pixels could be regarded as one new big pixel, our proposed method is also suitable for the other two cases: one DMD pixel being assigned to multiple CCD pixels, and multiple DMD pixels being assigned to one CCD pixel. Among the three cases, there is no obvious difference in the percentage of pixel-to-pixel alignment. The alignment accuracy of our proposed method is limited by the maximum resolution of SLM/CCD. According to Eqs. (29), (32)–(34), it is known that $\Delta\theta_1$, $\Delta\phi$ and $\Delta\varphi$ will be increased with the diminution of the maximum resolution. Compared with the maximum resolution of off-the-shelf SLM/CCD, the maximum resolution of the SLM/CCD used in experimental setup is relatively small. Our proposed method is faced with another limitation that it is only suitable for two grating elements. For more than two grating elements, it is feasible that these grating elements are aligned in pairs by our four-step alignment method.

References

[1] J. L. Suo, X. Y. Ji, and Q. H. Dai, "An overview of computational photography," *Sci. China Inf. Sci.*, vol. 55, no. 6, pp. 1229–1248, 2012.

[2] G. Wetzstein, I. Ihrke, D. Lanman, D. Lanman, and W. Heidrich, "Computational plenoptic imaging," *Comput. Graph. Forum*, vol. 30, no. 8, pp. 2397–2426, 2011.

[3] S. V. Adams and C. M. Harris, "Computational model of innate directional selectivity refined by visual experience," *Sci. Rep.*, vol. 5, 2015, Art. no. 12553.

[4] X. Cao *et al.*, "Computational snapshot multispectral cameras: Toward dynamic capture of the spectral world," *IEEE Signal Process. Mag.*, vol. 33, no. 5, pp. 95–108, Sep. 2016.

[5] S. Ri, M. Fujigaki, T. Matui, and Y. Morimoto, "Accurate pixel-to-pixel correspondence adjustment in a digital micromirror device camera by using the phase-shifting moire method," *Appl. Opt.*, vol. 45, no. 27, pp. 6940–6946, 2006.

[6] X. Lin, G. Wetzstein, Y. Liu, and Q. Hai, "Dual-coded compressive hyperspectral imaging," *Opt. Lett.*, vol. 39, no. 7, pp. 2044–2047, 2014.

[7] G. Bub, M. Tecza, M. Helmes, P. Lee, and P. Kohl, "Temporal pixel multiplexing for simultaneous high-speed, high-resolution imaging," *Nature Methods*, vol. 7, no. 3, pp. 209–211, 2010.

[8] Y. Zhao, Q. Chen, S. Zhou, G. Gu, and X. Sui, "Super-resolution imaging through scattering medium based on parallel compressed sensing," *IEEE Photon. J.*, vol. 9, no. 5, Oct. 2017, Art. no. 7803012.

[9] S. K. Nayar, V. Branzoi, and T. E. Boult, "Programmable imaging: towards a flexible camera," *Int. J. Comput. Vision*, vol. 70, no. 1, pp. 7–22, 2006.

[10] C. L. Di *et al.*, "A Moire-based four-channel focusing and leveling scheme for projection lithography," *IEEE Photon. J.*, vol. 6, no. 4, Aug. 2014, Art. no. 2800112.

[11] S. Zhou, Y. Fu, X. Tang, S. Hu, W. Chen, and Y. Yang, "Fourier-based analysis of moire fringe patterns of superposed gratings in alignment of nanolithography," *Opt. Exp.*, vol. 16, no. 11, pp. 7869–7880, 2008.

[12] S. Ri, S. Hayashi, S. Ogihara, and H. Tsuda, "Accurate full-field optical displacement measurement technique using a digital camera and repeated patterns," *Opt. Exp.*, vol. 22, no. 8, pp. 9693–9706, 2014.

[13] H. Miao *et al.*, "A universal moire effect and application in X-ray phase-contrast imaging," *Nature Phys.*, vol. 12, no. 9, pp. 830–834, 2016.

[14] Y. Zhou, J. P. Zhu, Q. Y. Deng, J. B. Liu, X. C. Si, and S. Hu, "Moire-based interferometry for magnification calibration of bitelecentric lens system," *IEEE Photon. J.*, vol. 7, no. 6, Dec. 2015, Art. no. 3900311.

[15] J. Zhu, S. Hu, J. Yu, and Y. Tang, "Alignment method based on matched dual-grating moiré fringe for proximity lithograph," *Opt. Eng.*, vol. 51, no. 11, 2012, Art. no. 113603.

[16] N. Wang *et al.*, "Influence of collimation on alignment accuracy in proximity lithography," *IEEE Photon. J.*, vol. 6, no. 4, Aug. 2014, Art. no. 2500010.

[17] E. E. Moon, L. Chen, P. N. Everett, M. K. Mondol, and H. I. Smith, "Interferometric-spatial-phase imaging for six-axis mask control," *J. Vac. Sci. Technol. B*, vol. 21, no. 6, pp. 3112–3115, 2003.

[18] S. Zhou, Y. Yang, L. Zhao, and S. Hu, "Tilt-modulated spatial phase imaging method for wafer-mask leveling in proximity lithography," *Opt. Lett.*, vol. 35, no. 18, pp. 3132–3134, 2010.

[19] Y. Tang, Y. He, Y. Yang, J. Wang, J. B. Liu, and W. Yan, "Nano-focusing and leveling system based on improved phase analysis," *IEEE Photon. J.*, vol. 8, no. 2, Apr. 2016, Art. no. 6802007.

[20] S. Ri, M. Fujigaki, T. Matui, and Y. Morimoto, "Pixel-to-Pixel Correspondence Adjustment in DMD Camera by Moire Methodology," *Exp. Mech.*, vol. 46, no. 1, pp. 67–75, 2006.

[21] I. Amidror and R. D. Hersch, "Fourier-based analysis of phase shifts in the superposition of periodic layers and their Moiré effects," *J. Opt. Soc. Amer. A*, vol. 13, no. 5, pp. 974–987, 1996.